An Acad Bras Cienc (2024) 96(Suppl. 1): e20230648 DOI 10.1590/0001-3765202420230648
Anais da Academia Brasileira de Ciências | *Annals of the Brazilian Academy of Sciences*
Printed ISSN 0001-3765 I Online ISSN 1678-2690
www.scielo.br/aabc | www.fb.com/aabcjournal

ENGINEERING SCIENCES

Experimental investigation of thermal runaway in 40Ah prismatic lithium batteries at different SOC

NINGNING WEI & MINGHAI LI

Abstract: With the evolution of energy storage, Thermal Runaway (TR) stands out as the most critical safety concern for Lithium-Ion Batteries (LIBs). This study employs a prismatic lithium battery with a nominal capacity of 40Ah, featuring $Li(Ni_{0.6}Co_{0.2}Mn_{0.2})O_2$ as the cathode material. The investigation delves into the thermal runaway characteristics of the battery at 25%, 50%, 75%, and 100% State of Charge (SOC) in a nitrogen environment. The findings indicate: 1) an ascending trend in the highest temperatures at various points within the battery as SOC increases, accompanied by a declining trend in normalized gas production and a non-linear relationship between the heat released during TR and the stored electrochemical energy; 2) the highest temperature point within the battery consistently resides at the surface, offering insights for the temperature monitoring of the Battery Thermal Management System (BTMS); 3) a direct correlation between higher SOC and increased material ejection, with a mass loss rate of 25.8% at 100% SOC, a static total gas production of 2.45 mol, and a maximum explosion index of 0.2886 $kPa{\cdot}m{\cdot}s^{-1}$.

Key words: Lithium-ion battery, thermal runaway, gas generation analysis, temperature.

INTRODUCTION

The rapid development of energy storage and new energy vehicles has generated significant demand for lithium-ion batteries (LIBs) (Ashwin et al. 2018). A large number of batteries are assembled into modules to power the operation of energy storage facilities. However, the widespread use of LIBs has led to an increase in fire incidents. It is important to note that the thermal runaway processes differ significantly among different individual battery cells. Furthermore, the thermal runaway mechanisms of batteries vary at different state of charge (SOC) levels. Investigating the propagation mechanisms of thermal runaway in batteries holds crucial significance in preventing and controlling fire incidents in energy storage facilities (Yang et al. 2018, Legrand et al. 2014, Li et al. 2018, Ren et al. 2018, Yang et al. 2017).

The characteristics of thermal runaway propagation in LIBs are influenced by various factors, including circuit connection methods, storage conditions, contact area, environmental temperature, and state of charge (SOC) (Broussely et al. 2005, Wang et al. 2011, Käbitz et al. 2013, Dubarry et al. 2018, Keil et al. 2016, Ecker et al. 2012). Hatchard et al. (Hatchard et al. 2001) utilized numerical simulations to uncover the thermal runaway process in single cylindrical lithium-ion batteries, revealing that as the battery volume increases, thermal runaway becomes more prone to occur. Huang et al. (Huang et al. 2016) investigated the influence of the diameter of individual cylindrical batteries on the onset temperature and duration of thermal runaway. The results demonstrated that within the range of diameters varying from 5 millimeters to 20

millimeters, the onset temperature of thermal runaway decreased from 440.3 K to 425.8 K.

The design and optimization of BTMS play a pivotal role in preventing thermal instability, achieving precision in controlling battery temperature through the judicious configuration of heat dissipation and temperature control systems (Talele et al. 2023a, Baveja et al. 2023, Fan et al. 2023). Numerous publicly disseminated experiments and models not only validate research hypotheses but also furnish guidance for the safety and reliability of future battery system designs. For instance, literature (Vashisht et al. 2023) enhances the electrothermal model from the perspective of discharge depth and temperature impact, literature (Singh et al. 2023, Feng et al. 2023) optimizes and computes the cooling performance of battery systems, literature (Talele et al. 2023b) computationally models and statistically evaluates the response of safety mechanisms to thermal instability in lithium-ion batteries, and literature (Talele et al. 2023c) employs phase-change materials to address strategies for mitigating propagation delays in battery thermal instability.

For accurate prediction of thermal runaway hazards in lithium-ion batteries, it is essential to consider the eruption process of LIBs, which can provide crucial research outcomes for thermal runaway warning systems and fire suppression strategies, such as onset time and release time (Liu et al. 2022, Yang et al. 2017). Several experts and scholars (Sharp et al. 2022, Chen et al. 2022, Huang et al. 2022, Feng et al. 2018) have investigated the categorization of the eruption process in LIBs. Photography is a commonly used method for delineating the eruption process. Zhang et al. (Zhang et al. 2020) selected a commercial prismatic battery in an electric vehicle with a nickel-manganese lithium cathode to study the initial eruption process of released products during thermal runaway. The experiments were conducted in a sealed chamber using nitrogen gas (N_2) as an inert protective environment to prevent combustion, and high-speed photography was employed to capture the rapid initial eruption process. Based on observations, the initial eruption process initially underwent an initial jet-like and conical eruption, followed by a prolonged amorphous eruption, and finally, an inverted conical eruption.

A meta-analysis of 76 experimental research papers on the potential effects of thermal runaway on lithium-ion batteries was conducted in reference (Rappsilber et al. 2023). The findings indicate that during thermal runaway, the total gas emissions from the battery, as a function of battery geometry, cathode active material, and state of charge (SOC), were determined to be 27 mmol/Wh for fully charged cylindrical lithium-ion batteries (with some unverifiable measurements reaching up to 48 mmol/Wh) (Rappsilber et al. 2023). For pouch and prismatic batteries, the total gas emissions were determined to be 30 mmol/Wh and 33 mmol/Wh, respectively. The analysis of released hydrogen fluoride (HF) gas content revealed that with an increase in battery charge state, the detected HF content decreases (Rappsilber et al. 2023). The highest detected HF content was 197 mg/Wh for fully charged pouch batteries and 175 mg/Wh for fully charged prismatic batteries (Rappsilber et al. 2023). This suggests that the fluorine content from fully charged batteries also enters other fluorine-containing compounds, rendering it unavailable for the formation of HF (Rappsilber et al. 2023).

The battery utilized in this study is a prismatic lithium-ion battery with $Li(Ni_{0.6}Co_{0.2}Mn_{0.2})O_2$ as the cathode material. Thermal runaway (TR) experiments were conducted on the battery in a 1000 L adiabatic test chamber under different state of charge (SOC) conditions, namely, 100%

SOC, 75% SOC, 50% SOC, and 25% SOC. To evaluate the TR characteristics, several key parameters were selected from the experiments, including the temperature of the safety valve nozzle, battery surface temperature, experimental chamber temperature, gas generation rate, and positive/negative electrode tab temperatures. The impact of SOC on the critical state of TR was analyzed, and high-speed cameras were used to capture videos of the moment of thermal runaway. Gas generation after TR, normalized gas generation, and mass loss rate were calculated. The findings of this research can provide valuable insights for the development of fire warning systems, fire suppression strategies, and storage considerations for batteries.

ABBREVIATIONS

TS = Cell side surface center temperature, °C
TE = Cell jet zone temperatures near the cell safety valve, °C
TA = Experimental chamber ambient temperature, °C
TP = Positive pole temperature, °C
TN = Negative pole temperature, °C
TH = Temperature at the center point of the heating plate °C
TR = Thermal runaway
DMC = Dimethyl carbonate, C3H6O3
EMC = Methyl ethyl carbonate, C4H8O3
HEV = Hybrid electric vehicle
EV = Electric vehicle
AEC = Constant volume adiabatic experimental chamber
PCM = Phase Change Material
T = time, s
OCV = Open circuit voltage
KLIB = Gas explosion index
LIB = Lithium-ion battery
BMS = Battery management system
BTMS = Battery thermal management system
SOC = State of charge
P = Pressure, kPa
C-rate = The charge and discharge current with respect to its nominal capacity
K = Mass loss rate

MATERIALS AND METHODS

Battery sample

The investigated samples in this study comprise lithium-ion batteries with Li $(Ni_{0.6}Co_{0.2}Mn_{0.2})$ O_2 as the cathode material, graphite as the anode material, and a $LiPF_6$-based electrolyte solution. The specific parameters of the battery samples are presented in Table I, and the Appendix, Table AI and AII.

Experimental instruments

The experimental setup employed in this study consists of four main components: the

Table I. Detailed technical specifications of the test cell.

Parameters	Specifications
Cell mass (g)	840
Size(mm)	20×173×120
Nominal capacity(V)	3.7
Maximum voltage(V)	4.2V
Minimum voltage (V)	2.7
Nominal capacity(Ah)	40 Ah
internal resistance(m ohm)	1.5
Cathode active material	$Li(Ni_{0.6}Co_{0.2}Mn_{0.2})O_2$
Anode active material	Graphite
Main components of electrolyte	DMC, EMC
Cathode current collector	Aluminum foil
Anode current collector	Copper foil
Shell Material	Aluminium alloy

experimental chamber, heating system, signal acquisition system, and inert gas replacement system.

The experimental chamber has a volume of 1000 L and is capable of withstanding a maximum pressure of 2 MPa. The chamber's door is hydraulically driven, enabling full internal sealing.

The heating system comprises a constant power heating plate with a power rating of 550 W, matching the size of the battery, to facilitate lateral heating and trigger thermal runaway. A quartz plate is employed as a thermal insulator. Additionally, a battery fixture is utilized to provide preloading force and structural support.

The signal acquisition system consists of various sensors for real-time monitoring within the experimental chamber. A pressure sensor (HM90) with an accuracy of ±0.25% full scale (FS) is employed to continuously monitor the chamber pressure (P). A voltage sensor is used to measure the battery voltage in real-time. Eight K-type thermocouples (WRNK191) with an accuracy of ±2.5 °C or ±0.75% of the temperature at the tabs are used for real-time monitoring of the temperature at different points within the battery and the ambient temperature within the experimental chamber. The thermocouple (T_S) is placed at the center of the battery's larger surface to measure the battery's surface temperature. The thermocouple (T_H) is positioned at the center of the battery and heating plate to measure their temperatures in real-time. The thermocouple (T_E) is placed 4 cm directly above the safety valve to measure the temperature in the ejection zone. Three thermocouples (T_{A1}, T_{A2}, and T_{A3}) are positioned 40 cm away from the battery at different locations within the experimental chamber to measure the ambient temperature. By averaging the data from these three thermocouples (T_{A1}, T_{A2}, and T_{A3}), the average ambient temperature (Ambient average temperature TA) can be obtained. The sampling frequency of the temperature sensors is set at 10 Hz. The process of thermal runaway eruption in lithium-ion batteries at 50% SOC, 75% SOC, and 100% SOC was recorded using a high-speed camera (model: ACS-3) from nac, Japan, capturing the process at 5000 frames per second.

The inert gas replacement system operates as follows: N_2 is introduced into the experimental chamber through an intake pipeline, while the chamber's gas is expelled through an exhaust pipeline. The vacuum pump provides the power to replace the gas within the chamber. N_2 serves three purposes: 1) acting as a carrier gas to create a dry and inert oxygen-free atmosphere, 2) preventing the risk of fire within the reaction vessel, and 3) controlling the temperature of the released gas within the reaction vessel to a manageable level.

The detailed structure of the experimental setup is illustrated in Figure 1.

Experimental procedure

Prior to the commencement of the experiments, the batteries were subjected to charging and discharging cycles using a battery testing system (NEWARE CT-4008, 5V/6A). The charging process was conducted at a constant current-constant voltage (CCCV) mode, with a current of 1/3 C, until reaching a voltage of 4.2 V. Subsequently, the batteries were left undisturbed for a period of 3 hours. The discharging process was then initiated at a constant current (CC) mode, with a current of 1/3 C, until reaching a voltage of 2.5 V. Once again, the batteries were left undisturbed for a period of 3 hours. This discharge and charge cycle was repeated three times for each battery. Following these cycles, the batteries were charged using the CCCV mode to reach different state-of-charge (SOC) levels, namely 100%, 75%, 50%, and 25%. Subsequently, the batteries were

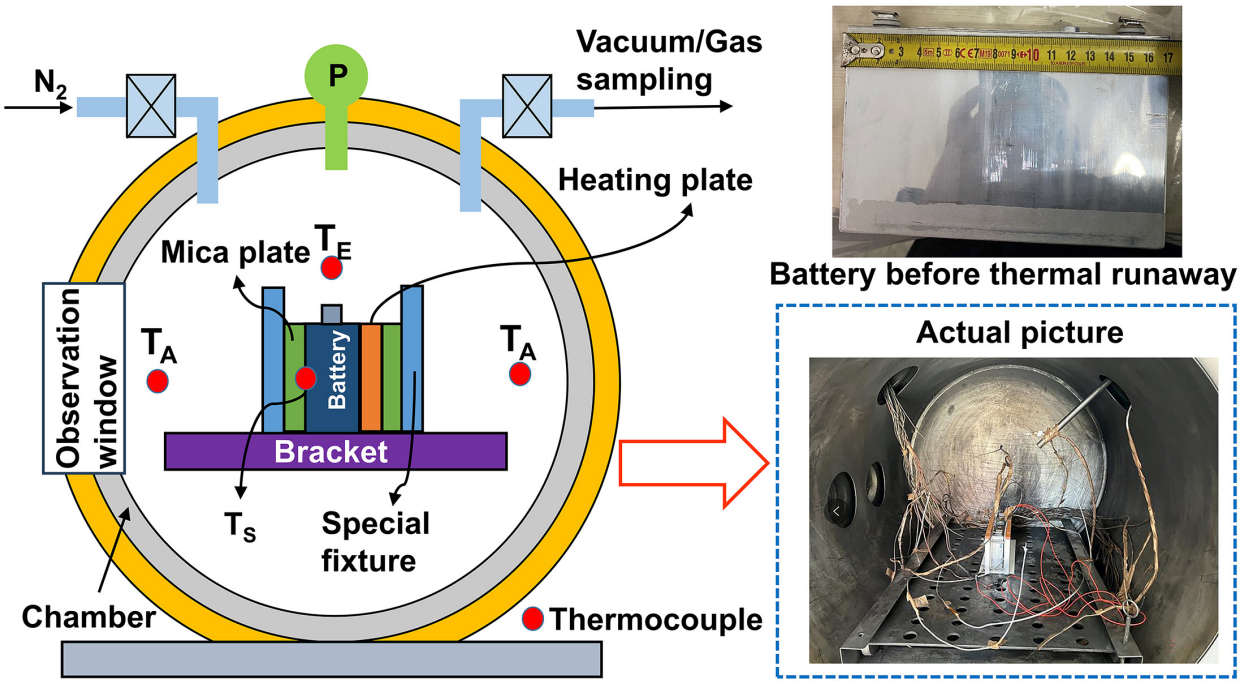

Figure 1. Structure diagram of the experimental chamber.

allowed to rest for 24 hours, and their weights were measured to mitigate the influence of internal heating between the charging and discharging processes. Mechanical constraints were applied to the front and back walls of the battery casing using mica mechanical fixtures.

Experimental Setup: The battery was positioned within the Advanced Energy Conversion (AEC) facility, accompanied by the arrangement of a thermocouple and insertion of a heating element. Simultaneously, the clamping force of the fixture was adjusted. The structural configuration of the experimental fixture consisted of a metallic clamp, thermal insulation pad, heating element, battery cell, insulation pad, and metallic clamp, in that order. A thermal insulation pad was placed beneath the bottom of the battery, as depicted in Figure 1.

Instrument Inspection: The heating element circuitry was examined to verify its proper functioning, followed by a check of the temperature and pressure data acquisition system for normal operation. Subsequently, the AEC chamber door was closed, and the vacuuming and nitrogen injection procedures were repeated three times, reaching a vacuum pressure of 15 kPa and nitrogen pressure of approximately 106 kPa, ensuring that the oxygen content in the test environment was below 1% (as confirmed by sampling tests). After each vacuuming and nitrogen injection cycle, a 5-minute settling period was observed to allow the temperature and pressure within the AEC chamber to stabilize.

Heating of the Heating Plate: The heating plate was activated to maintain a heating rate of 2 °C/min for the heating element, employing a transverse heating approach to induce the battery to enter the thermal runaway (TR) state. Throughout this testing process, both temperature and pressure exhibit an upward trend. As the battery temperature rises and reaches a certain threshold, the internal chemical reaction rate accelerates, signifying the onset of thermal runaway (determined in this

study as the point of voltage drop to zero). At this stage, heating is halted, and the moment of thermal runaway is captured using a high-speed camera. Once the battery has cooled to ambient temperature, the chamber door is opened for photographic documentation, followed by the removal of the battery for weighing, thereby concluding the experimental procedure.

Criterion for the Termination of Smoke Release in Battery Thermal Runaway: Following the occurrence of thermal runaway, the fluctuation rate of the gas pressure within the combustion chamber is maintained below $dP/dt < 0.2$ kPa/s for a duration exceeding 3 seconds. The test concludes 30 minutes after the voltage reaches 0V. Data acquisition involves sampling temperature, pressure, and heating element power, with a sampling frequency of ≥10Hz.

Post-experiment Conclusion: Subsequent to the completion of the experiment, the remaining portion of the battery (solely comprising the battery core) was meticulously photographed and weighed. The battery remnants were hermetically sealed in sample bags to ensure their preservation. Additionally, an assortment of ejections (including dispersed powders, particles, aluminum foil, electrode plates, among others) resulting from the battery's eruption were meticulously collected and subjected to weighing procedures.

RESULTS AND DISCUSSION

Temperature and voltage changes in TR experiments

Figure 2 displays the photograph of the battery after thermal runaway (TR), Figure 2(a) shows the photo after 100% SOC thermal runaway, Figure 2(b) shows the photo after 75% SOC thermal runaway, Figure 2(c) shows the photo after 50% SOC thermal runaway, and Figure 2(d) shows the photo after 25% SOC thermal runaway. In Figure 2, a substantial amount of viscous material

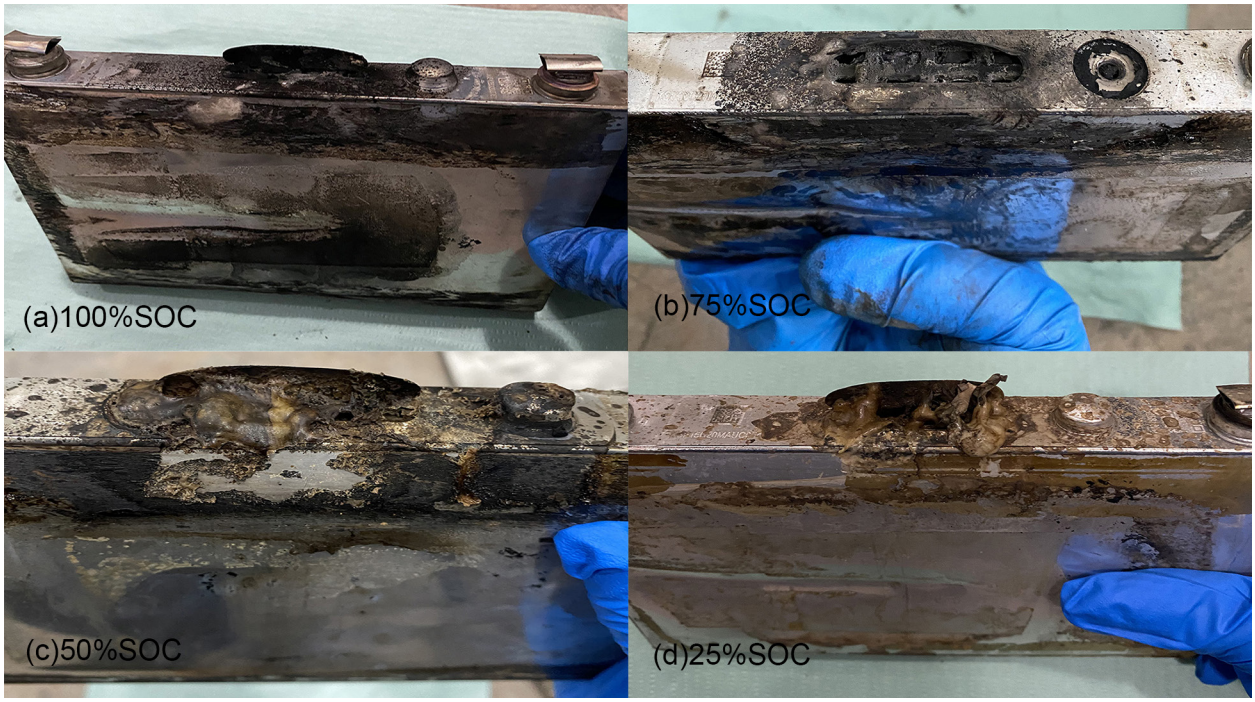

Figure 2. Photo of the battery after TR. (a) Photo of the battery after thermal runaway at 100% SOC, (b)Photo of the battery after thermal runaway at 75% SOC, (c) Photo of the battery after thermal runaway at 50% SOC, (d) Photo of the battery after thermal runaway at 25% SOC.

from the battery's interior can be observed at the safety valve outlet of the batteries with 50% state of charge (SOC) and 25% SOC. However, no traces of melted aluminum were found based on the visual examination of Figure 2. Moreover, considering the data collected from the thermocouples positioned on the battery surface, a comprehensive analysis indicates that the battery surface temperature did not reach the melting point of aluminum (660 °C). This finding contrasts with the observations of melted aluminum in TR experiments reported in other referenced literature (Walker et al. 2019).

Figure 3 illustrates the temperature and voltage variations of the battery during the thermal runaway (TR) process under different state of charge (SOC) conditions. Analyzing the curves depicted in Figure 3, the TR process can be divided into four distinct stages, each characterized by three critical temperatures (Feng et al. 2014).

Stage 1: During this initial stage, characterized by a battery self-heating rate below 0.02 °C/min, the battery experiences a decline in capacity accompanied by a slight decrease in voltage (Feng et al. 2014).

Stage 2: T_1 represents the onset temperature of self-generated heat within the battery (Feng et al. 2014). As the temperature rises, the decomposition of the solid electrolyte interface (SEI) occurs. Additionally, the anode, which loses the protective SEI film, initiates reactions with

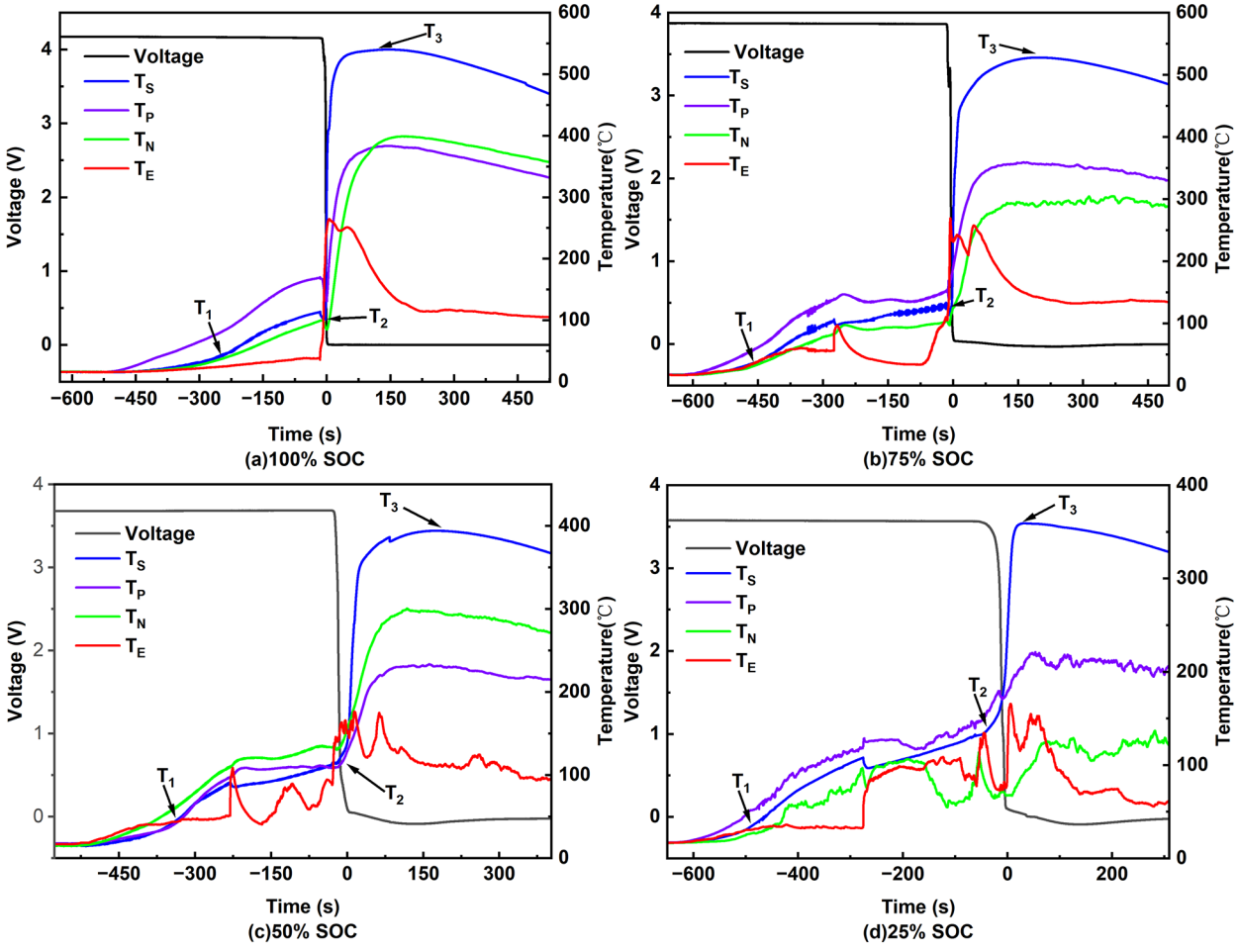

Figure 3. Voltage and temperature variation with time during TR.

the electrolyte (Ryou et al. 2012, Yang & Shen 2007), resulting in the release of heat and a gradual increase in battery temperature.

Stage 3: T_2 represents the triggering temperature of the battery, defined as the self-heating rate exceeding 1 °C/s. At elevated temperatures, various chemical reactions within the battery generate a significant amount of gas, leading to an increase in internal pressure. When the internal pressure reaches a critical threshold, the safety valve opens to release the pressure (Mao et al. 2020). As the gas is expelled, the battery temperature experiences a slight decrease. Subsequently, heat is released from chemical reactions within the battery materials, such as SEI decomposition, cathode decomposition, and reactions between the anode and electrolyte (Mao et al. 2020), resulting in a gradual temperature rise. Additionally, as the temperature increases, the chemical reaction rate further accelerates, leading to a faster rise in battery temperature (Yang et al. 2022).

Stage 4: T_3 represents the highest temperature attained during the thermal runaway (TR) process, defined as the peak temperature reached within the process (Feng et al. 2014). In the transition from T_2 to T_3, which corresponds to the fourth stage, internal chemical reactions within the battery intensify, including cathode decomposition, reactions between the anode and electrolyte, and electrolyte decomposition (Mao et al. 2020). These reactions release a substantial amount of heat, leading to a rapid increase in battery temperature.

Based on the observations in Figure 3, it is evident that during the progression from heating to the conclusion of thermal runaway, the temperature data collected by the thermocouples at the same time point exhibit the order: $T_S > T_P > T_N > T_E$ for batteries at different states of charge (SOC). As the SOC decreases, the temperature curves of T_P, T_N, and T_E demonstrate an increasing level of variability during the second stage.

According to the existing literature, various chemical reactions occur in the positive electrode material within the temperature range of 100-300 °C. The graphite crystal structure undergoes collapse and deformation, while LiC_6 and Li_xSi react with the electrolyte, releasing heat (Wang et al. 2022, Liu et al. 2020). Both crystalline and amorphous forms of silicon transform into amorphous phases during the lithium intercalation process and subsequently convert back into crystalline compounds (Li et al. 2019). Within the temperature range of 110-300 °C, the cathode undergoes a series of phase transitions, transitioning from a layered structure to M_3O_4 spinel and finally to rock salt (Li et al. 2021, Liu et al. 2020). Both of these processes involve the release of a substantial amount of oxygen, which reacts with the electrolyte and releases a significant amount of heat (Zhang et al. 2019).

Plotting $T_{S,max}$, $T_{P,max}$, $T_{N,max}$, and $T_{E,max}$ for different states of charge (SOC) yields Figure 4. From Figure 4, it is evident that the values of $T_{S,max}$, $T_{P,max}$, $T_{N,max}$, and $T_{E,max}$ increase with increasing SOC. Among the thermocouples in batteries at different SOC levels, TS corresponds

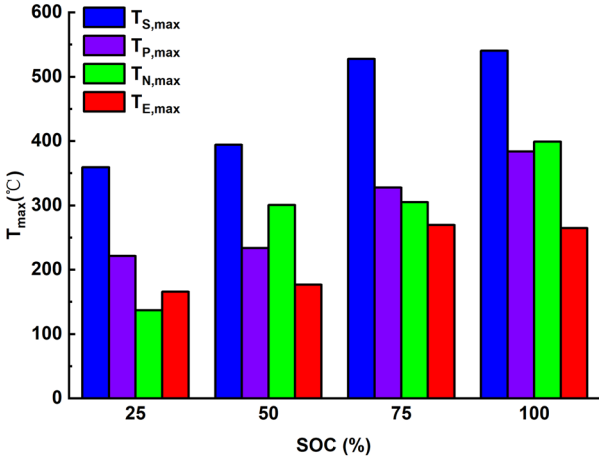

Figure 4. Maximum Temperature at Different Measurement Points.

to the highest temperature point, while $T_{E,max}$ represents the lowest temperature point at 100% SOC, 75% SOC, and 50% SOC. At 25% SOC, $T_{N,max}$ indicates the lowest temperature point.

Handling of pressure rise rate

Due to the significant thermodynamic changes induced by battery cell rupture, the temporal evolution of pressure within the sealed compartment is presented in Figure 5. As depicted in Figure 5, it is observed that over time, the pressure inside the chamber exhibits an initial gradual and steady increase, attributed to the temperature rise. Subsequently, the pressure experiences a rapid surge followed by a sharp decline, eventually reaching a nearly constant value. The primary factor contributing to the internal pressure increase in the battery is the generation of gases, as summarized in the literature (Golubkov et al. 2015, Wang et al. 2019).

In order to obtain a standardized pressure rise rate curve for lithium-ion battery (LIB) eruption, this study introduces the concept of LIB eruption index (K_{LIB}) proposed in literature (Wang et al. 2022) and utilizes Equation (1) to calculate K_{LIB}, resulting in a time-varying curve as depicted in Figure 5. During the calculation process, Equation (2) is employed to determine the maximum value of KLIB.

$$K_{LIB} = (dP/dt)V^{1/3} \quad (1)$$

where dP/dt refers to the rate at which the pressure inside the chamber increases over time

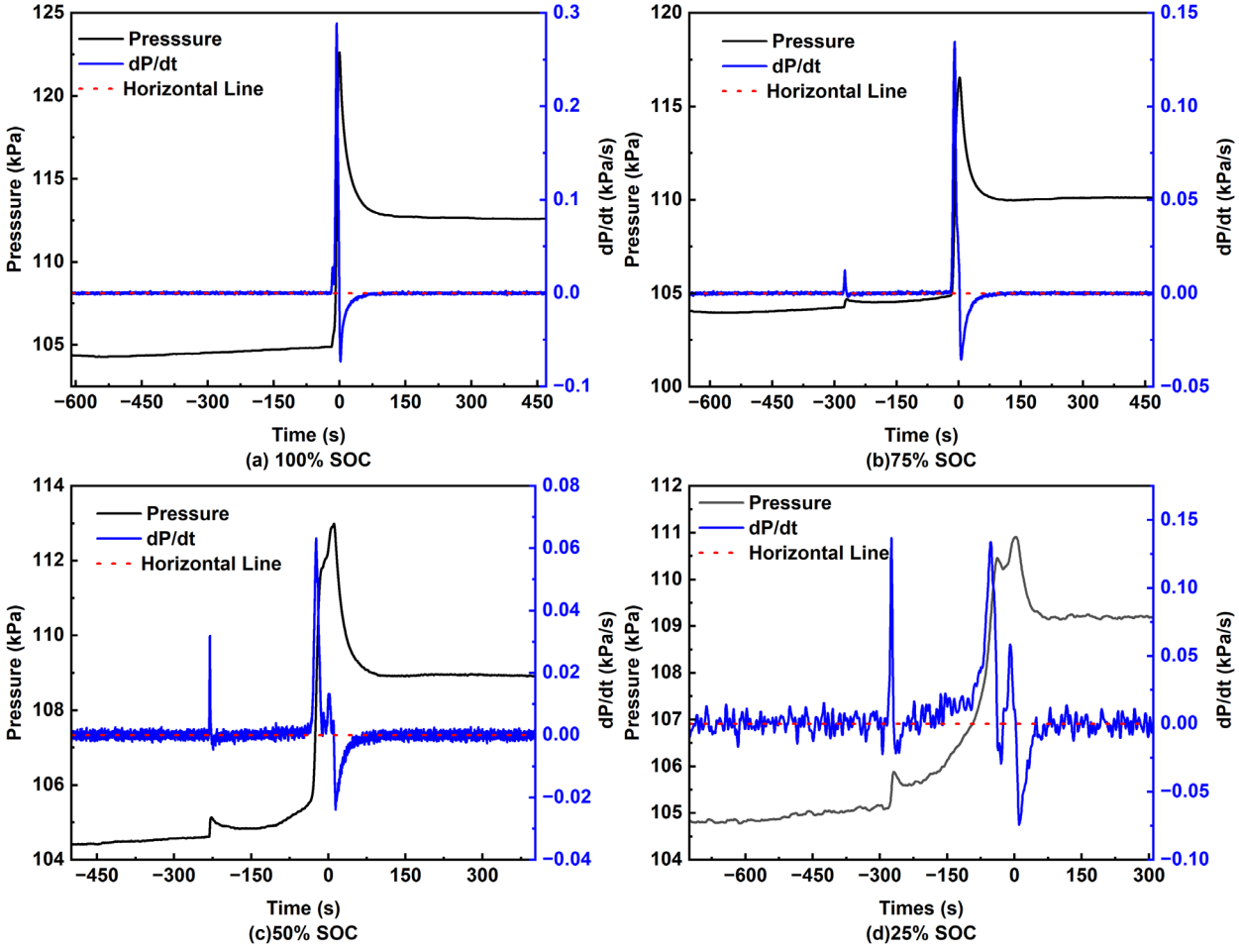

Figure 5. Pressure and dP/dt with time.

during LIB spraying, and V refers to the volume of the sealed chamber.

$$K_{LIB,max} = (dP/dt)_{max} V^{1/3} \quad (2)$$

The term $K_{LIB,max}$ refers to the maximum value of K_{LIB}, while $(dP/dt)_{max}$ represents the maximum rate of pressure increase within the chamber (Wang et al. 2022). To effectively compare the $K_{LB,max}$ values of batteries at different initial SOC, measurements should be conducted under identical conditions using containers of the same shape and volume. Specifically, the $K_{LB,max}$ value for the battery at 100% SOC is 0.2886 kPa·m·s^{-1}, while for the battery at 75% SOC, it is 0.1345 kPa·m·s^{-1}. The battery at 50% SOC exhibits a $K_{LB,max}$ value of 0.0632 kPa·m·s^{-1}, and the battery at 25% SOC has a $K_{LB,max}$ value of 0.1266 kPa·m·s^{-1}. Figure 5 illustrates that the K_{LIB} curves of the battery safety valve jet are more sensitive to SOC. Moreover, the videos captured by a high-speed camera confirm that lower SOC levels result in a greater emission of substances prior to thermal runaway.

Quality loss rate and gas production

To investigate the relationship between the scale of thermal runaway events and the quantity of expelled materials, a comparison of mass characteristics and gas generation rates before and after battery experiments reveals that more intense thermal runaway events are typically associated with larger mass ejections.

The test results demonstrate a significant gas generation from TR. Furthermore, the electrolyte in the battery also vaporizes at high temperatures, yielding large molecular organic compounds. Despite the four batteries being identical, experimental findings reveal substantial variations in gas generation rates. The gas evolution rate of the battery is delineated by Equations (3) and Equations (4) (Wei & Li 2023).

$$PV = nRT \quad (3)$$

$$n = \frac{P_2 V_2}{R T_2} - n_0 \quad (4)$$

where, n represents the gas yield, P_2 denotes the real-time pressure within the compartment after TR, V_2 signifies the volume of the experimental chamber, R represents the ideal gas constant, T_2 signifies the stabilized environmental temperature within the experimental chamber, and n_0 represents the initial volume of gas within the chamber.

Due to the rapid increase in temperature and pressure of the battery following TR, precise gas measurements can only be obtained when the temperature and pressure within the experimental chamber stabilize. Table II presents the experimental data obtained after achieving stable temperature (T_A is the relative temperature) and pressure conditions within the experimental cabin.

To facilitate the analysis of the energy required for the temperature rise of the gases inside the experimental chamber, certain assumptions were made: (1) the specific heat capacity of the gases before and after the experiment is considered constant at 0.741 J/(g*K) (consistent with nitrogen's constant volume specific heat capacity); (2) all energy released externally during thermal runaway contributes to the temperature rise of the experimental chamber. Based on these assumptions, the released energy during thermal runaway can

Table II. Experimental results of thermal runaway under different SOC conditions.

SOC	K	Gas production (mol)	T_A(°C)
100%	0.26	2.45	13.0
75%	0.23	2.06	10.5
50%	0.21	1.35	9.5
25%	0.20	1.52	6.4

be calculated as 12.7 kJ, 10.2 kJ, 9.1 kJ, and 6.1 kJ for 100% SOC, 75% SOC, 50% SOC, and 25% SOC, respectively. These values are normalized and plotted in Figure 6 (Rappsilber et al. 2023). Additionally, the gas production of the battery has been normalized (Yang et al. 2022) and plotted in Figure 6.

The computation formula for the mass loss rate (K) in Table II is expressed by Equation (5), as delineated below (Wei & Li 2023):

$$K = \frac{m_e}{m_r} \times 100\% \quad (5)$$

where K is the mass loss rate, m_r is the initial mass of the battery, m_e is the residual weight of the battery after TR.

From Table II and Figure 6, it is evident that both the mass loss rate and gas production increase with increasing state of charge (SOC). However, when considering the normalized gas production, it is apparent that the gas production does not maintain a linear relationship with the stored electrochemical energy.

CONCLUSIONS

In the pursuit of investigating the initial temperature distribution of the battery jet and its variation with State of Charge (SOC) in a nitrogen environment, the thermal runaway of a 40Ah prismatic cell was induced through external heating. The primary conclusions are summarized as follows:

(1) Video footage captured by a high-speed camera reveals that, with the decrease in State of Charge (SOC), there is an increase in the material ejected from the battery before Thermal Runaway (TR). As the SOC value increases, TS, TP, TN, and TE exhibit an ascending trend. The maximum detected value of KLIB occurs at 100% SOC, reaching 0.2886 kPa·m·s^{-1}.

(2) At 100% State of Charge (SOC), the highest temperature in the ejection zone surpasses the temperature on the battery surface. Across SOC values of 25%, 50%, 75%, and 100%, the temperature on the battery surface exceeds temperatures at other locations, indicating the influence of SOC on the temperature distribution during battery thermal runaway.

(3) As the State of Charge (SOC) of the battery increases, there is a corresponding rise in the total gas production; however, the normalized gas production exhibits a declining trend. Furthermore, the overall Thermal Runaway (TR) energy release does not maintain a linear relationship with the electrochemical energy stored.

Limitations of the Experiment: Reduction in the experimental chamber volume or an increase in battery capacity may lead to an elevated explosion index, K. A comparison with the outcomes presented in references (Yang et al. 2022) and (Rappsilber et al. 2023) reveals an 83-fold reduction in volume, resulting in an exponential increase in explosion indices of 408 times (NCM523) and 269 times (NCM622). Due to experimental constraints, the current study did not delve into the analysis of the impact of the experimental chamber volume on the explosion index, K. Additionally, the influence of preload force on thermal runaway behavior was not considered. As indicated in reference (Wei &

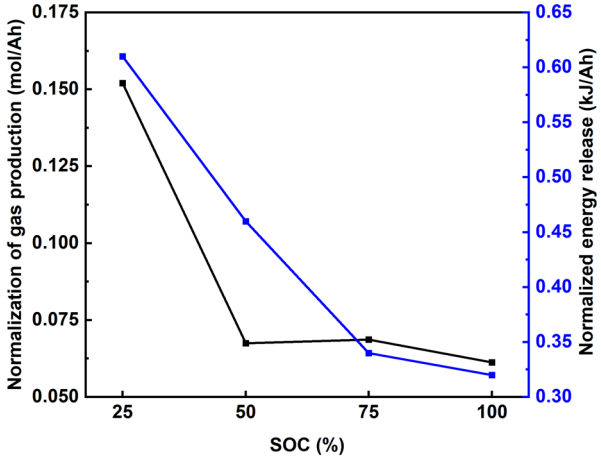

Figure 6. Energy release and gas production.

Li 2023), preload force significantly affects the thermal runaway and gas generation behaviors of lithium-ion batteries. Nevertheless, the current understanding of the safety implications of preload force on lithium batteries remains unclear.

REFERENCES

ASHWIN TR, BARAI A, UDDIN K, SOMERVILLE L, MCGORDON A & MARCO J. 2018. Prediction of battery storage ageing and solid electrolyte interphase property estimation using an electrochemical model. J Power Sources 385: 141-147.

BAVEJA R, BHATTACHARYA J, PANCHAL S, FRASER R & FOWLER M. 2023. Predicting temperature distribution of passively balanced battery module under realistic driving conditions through coupled equivalent circuit method and lumped heat dissipation method. J Energy Storage 70: 107967.

BROUSSELY M, BIENSAN Ph, BONHOMME F, BLANCHARD PH, HERREYRE S, NECHEV K & STANIEWICZ RJ. 2005. Main aging mechanisms in Li ion batteries. J Power Sources 146: 90-96.

CHEN S, ZHANG G, ZHU J, FENG X, WEI X, OUYANG M & DAI H. 2022. Multi-objective optimization design and experimental investigation for a parallel liquid cooling-based Lithium-ion battery module under fast charging. Appl Therm Eng 211: 118503.

DUBARRY M, QIN N & BROOKER P. 2018. Calendar aging of commercial Li-ion cells of different chemistries – A review. Curr Opin Electrochem 9: 106-113.

ECKER M, GERSCHLER JB, VOGEL J, KÄBITZ S, HUST F, DECHENT P & SAUER DU. 2012. Development of a lifetime prediction model for lithium-ion batteries based on extended accelerated aging test data. J Power Sources 215: 248-257.

FAN Y, WANG Z, XIONG X, PANCHAL S, FRASER R & FOWLER M. 2023. Multi-Objective Optimization Design and Experimental Investigation for a Prismatic Lithium-Ion Battery Integrated with a Multi-Stage Tesla Valve-Based Cold Plate. Processes 11: 1618.

FENG X, FANG M, HE X, OUYANG M, LU L, WANG H & ZHANG M. 2014. Thermal runaway features of large format prismatic lithium ion battery using extended volume accelerating rate calorimetry. J Power Sources 255: 294-301.

FENG X, HE X, OUYANG M, WANG L, LU L, REN D & SANTHANAGOPALAN S. 2018. A Coupled Electrochemical-Thermal Failure Model for Predicting the Thermal Runaway Behavior of Lithium-Ion Batteries. J Electrochem Soc 165: A3748-A3765.

FENG Z, ZHAO J, GUO C, PANCHAL S, XU Y, YUAN J, FRASER R & FOWLER M. 2023. Optimization of the Cooling Performance of Symmetric Battery Thermal Management Systems at High Discharge Rates. Energy Fuels 37: 7990-8004.

GOLUBKOV AW, SCHEIKL S, PLANTEU R, VOITIC G, WILTSCHE H, STANGL C, FAULER G, THALER A & HACKER V. 2015. Thermal runaway of commercial 18650 Li-ion batteries with LFP and NCA cathodes – impact of state of charge and overcharge. RSC Adv 5: 57171-57186.

HATCHARD TD, MACNEIL DD, BASU A & DAHN JR. 2001. Thermal Model of Cylindrical and Prismatic Lithium-Ion Cells. J Electrochem Soc 148: A755.

HUANG L, LU T, XU G, ZHANG X, JIANG Z, ZHANG Z, WANG Y, HAN P, CUI G & CHEN L. 2022. Thermal runaway routes of large-format lithium-sulfur pouch cell batteries. Joule 6: 906-922.

HUANG P, PING P, LI K, CHEN H, WANG Q, WEN J & SUN J. 2016. Experimental and modeling analysis of thermal runaway propagation over the large format energy storage battery module with Li4Ti5O12 anode. Appl Energy 183: 659-673.

KÄBITZ S, GERSCHLER JB, ECKER M, YURDAGEL Y, EMMERMACHER B, ANDRÉ D, MITSCH T & SAUER DU. 2013. Cycle and calendar life study of a graphite|LiNi1/3Mn1/3Co1/3O2 Li-ion high energy system. Part A: Full cell characterization. J Power Sources 239: 572-583.

KEIL P, SCHUSTER SF, WILHELM J, TRAVI J, HAUSER A, KARL RC & JOSSEN A. 2016. Calendar Aging of Lithium-Ion Batteries: I. Impact of the Graphite Anode on Capacity Fade. J Electrochem Soc 163: A1872-A1880.

LEGRAND N, KNOSP B, DESPREZ P, LAPICQUE F & RAËL S. 2014. Physical characterization of the charging process of a Li-ion battery and prediction of Li plating by electrochemical modelling. J Power Sources 245: 208-216.

LI H, KONG X, LIU C & ZHAO J. 2019. Study on thermal stability of nickel-rich/silicon-graphite large capacity lithium ion battery. Appl Therm Eng 161: 114144.

LI J-F, LIN C-H & CHEN K-C. 2018. Cycle Life Prediction of Aged Lithium-Ion Batteries from the Fading Trajectory of a Four-Parameter Model. J Electrochem Soc 165: A3634-A3641.

LI Y ET AL. 2021. Thermal runaway mechanism of lithium-ion battery with LiNi0.8Mn0.1Co0.1O2 cathode materials. Nano Energy 85: 105878.

LIU C, LI H, KONG X & ZHAO J. 2020. Modeling analysis of the effect of battery design on internal short circuit hazard in

LiNi0.8Co0.1Mn0.1O2/SiOx-graphite lithium ion batteries. Int J Heat Mass Transf 153: 119590.

LIU J, PENG W, YANG M, JIN K, LIU P, SUN J & WANG Q. 2022. Quantitative analysis of aging and detection of commercial 18650 lithium-ion battery under slight overcharging cycling. J Clean Prod 340: 130756.

MAO B, HUANG P, CHEN H, WANG Q & SUN J. 2020. Self-heating reaction and thermal runaway criticality of the lithium ion battery. Int J Heat Mass Transf 149: 119178.

RAPPSILBER T, YUSFI N, KRÜGER S, HAHN S-K, FELLINGER T-P, KRUG VON NIDDA J & TSCHIRSCHWITZ R. 2023. Meta-analysis of heat release and smoke gas emission during thermal runaway of lithium-ion batteries. J Energy Storage 60: 106579.

REN D, SMITH K, GUO D, HAN X, FENG X, LU L, OUYANG M & LI J. 2018. Investigation of Lithium Plating-Stripping Process in Li-Ion Batteries at Low Temperature Using an Electrochemical Model. J Electrochem Soc 165: A2167-A2178.

RYOU M-H, LEE J-N, LEE DJ, KIM W-K, JEONG YK, CHOI JW, PARK J-K & LEE YM. 2012. Effects of lithium salts on thermal stabilities of lithium alkyl carbonates in SEI layer. Electrochimica Acta 83: 259-263.

SHARP M ET AL. 2022. Thermal Runaway of Li-Ion Cells: How Internal Dynamics, Mass Ejection, and Heat Vary with Cell Geometry and Abuse Type. J Electrochem Soc 169: 020526.

SINGH LK, KUMAR R, GUPTA AK, SHARMA AK & PANCHAL S. 2023. Computational study on hybrid air-PCM cooling inside lithium-ion battery packs with varying number of cells. J Energy Storage 67: 107649.

TALELE V, MORALI U, PATIL MS, PANCHAL S, FRASER R, FOWLER M, THORAT P & GOKHALE YP. 2023b. Computational modelling and statistical evaluation of thermal runaway safety regime response on lithium-ion battery with different cathodic chemistry and varying ambient condition. Int Commun Heat Mass Transf 146: 106907.

TALELE V, MORALI U, PATIL MS, PANCHAL S & MATHEW K. 2023a. Optimal battery preheating in critical subzero ambient condition using different preheating arrangement and advance pyro linear thermal insulation. Therm Sci Eng Prog 42: 101908.

TALELE V, PATIL MS, PANCHAL S, FRASER R & FOWLER M. 2023c. Battery thermal runaway propagation time delay strategy using phase change material integrated with pyro block lining: Dual functionality battery thermal design. J Energy Storage 65: 107253.

VASHISHT S, RAKSHIT D, PANCHAL S, FOWLER M & FRASER R. 2023. Thermal behaviour of Li-ion battery: An improved electrothermal model considering the effects of depth of discharge and temperature. J Energy Storage 70: 107797.

WALKER WQ, DARST JJ, FINEGAN DP, BAYLES GA, JOHNSON KL, DARCY EC & RICKMAN SL. 2019. Decoupling of heat generated from ejected and non-ejected contents of 18650-format lithium-ion cells using statistical methods. J Power Sources 415: 207-218.

WANG H, ZHANG Y, LI W, GAO Z, ZHANG B & OUYANG M. 2022. Experimental study on the cell-jet temperatures of abused prismatic Ni-rich automotive batteries under medium and high states of charge. Appl Therm Eng 202: 117859.

WANG J, LIU P, HICKS-GARNER J, SHERMAN E, SOUKIAZIAN S, VERBRUGGE M, TATARIA H, MUSSER J & FINAMORE P. 2011. Cycle-life model for graphite-LiFePO4 cells. J Power Sources 196: 3942-3948.

WANG Q, MAO B, STOLIAROV SI & SUN J. 2019. A review of lithium ion battery failure mechanisms and fire prevention strategies. Prog Energy Combust Sci 73: 95-131.

WEI N & LI M. 2023. Experimental study of thermal runaway process of 256Ah prismatic nickel-rich battery. Front Energy Res 11: 1230429.

YANG F, WANG D, ZHAO Y, TSUI K-L & BAE SJ. 2018. A study of the relationship between coulombic efficiency and capacity degradation of commercial lithium-ion batteries. Energy 145: 486-495.

YANG H & SHEN X-D. 2007. Dynamic TGA–FTIR studies on the thermal stability of lithium/graphite with electrolyte in lithium-ion cell. J Power Sources 167: 515-519.

YANG X ET AL. 2022. Experimental Study on Thermal Runaway Behavior of Lithium-Ion Battery and Analysis of Combustible Limit of Gas Production. Batteries 8: 250.

YANG X-G, LENG Y, ZHANG G, GE S & WANG C-Y. 2017. Modeling of lithium plating induced aging of lithium-ion batteries: Transition from linear to nonlinear aging. J Power Sources 360: 28-40.

ZHANG Y, WANG H, LI W, LI C & OUYANG M. 2019. Size distribution and elemental composition of vent particles from abused prismatic Ni-rich automotive lithium-ion batteries. J Energy Storage 26: 100991.

ZHANG Y, WANG H, LI W, LI C & OUYANG M. 2020. Quantitative analysis of eruption process of abused prismatic Ni-rich automotive batteries based on in-chamber pressure. J Energy Storage 31: 101617.

APPENDIX A

Table AI. The battery charging current limit at different temperatures.

Cell Temperature Range	−5 °C ≤ T < 5 °C	5 °C ≤ T < 10 °C	10 °C ≤ T < 23 °C	23 °C ≤ T < 40 °C	40 °C ≤ T ≤ 55 °C
Maximum charging current allowed	0.1 C				
Charging voltage limit (V)	4.05	4.15	4.25	4.25	4.25

Table AII. The battery discharging current and voltage limit at different temperatures.

Cell Temperature Range	−30 °C ≤ T< −20 °C	−20 °C ≤ T < 0 °C	0 °C ≤ T < 10 °C	10 °C ≤ T< 23 °C	23 °C ≤ T< 40 °C	40 °C ≤ T≤ 55 °C
Maximum charging current allowed	0.2 C	0.3 C	0.8 C	1 C	0.8 C	0.8 C
Discharging voltage limit (V)	2.0	2.5	2.75	2.75	2.75	2.75

How to cite
WEI N & LI M. 2024. Experimental investigation of thermal runaway in 40Ah prismatic lithium batteries at different SOC. An Acad Bras Cienc 96: e20230648. DOI 10.1590/0001-3765202420230648.

Manuscript received on June 07, 2023;
accepted for publication on March 04, 2024

NINGNING WEI
https://orcid.org/0009-0000-6888-6192

MINGHAI LI
https://orcid.org/0009-0001-8259-7730

Dalian Jiaotong University, College of Locomotive and Rolling Stock Engineering, Dalian 116028, China

Correspondence to: **Ningning Wei**
E-mail: 1716@sdp.edu.cn

Author contributions

Ningning Wei: Conceptualization, Methodology, Software. Ningning Wei: Data curation, Writing-Original draft preparation. Ningning Wei: Visualization, Investigation. Minghai Li: Supervision. Ningning Wei: Software, Validation. Minghai Li: Writing-Reviewing and Editing. All authors reviewed the manuscript.